Band-Renormalization Effects on Superconductivity and Antiferromagnetism in Two-Dimensional t-J Model

Ryo Sato[*] and Hisatoshi Yokoyama

Department of Physics, Tohoku University, Sendai 980-8578, Japan

Coexistence or exclusivity of $d_{x^2-y^2}$-wave superconducting (d-SC) and antiferromagnetic (AF) orders and instability toward phase separation (PS) are reconsidered for the square-lattice t-J model with the diagonal transfer (t') term near half filling. To reliably treat the strong correlation including the local constraint of no double occupancy, we use a variational Monte Carlo method, in which band-renormalization effect (BRE) is also incorporated. The results are compared with those of the corresponding Hubbard model recently obtained [J. Phys. Soc. Jpn. **85**, 074701 (2016)]. It is found that BRE is very effective for the AF order and greatly modifies the ground-state phase diagram in the t'-δ space (δ: doping rate), especially for large $|t'/t|$, proposed by previous studies; in a wide range of t'/t ($|t'/t| \leq 0.5$) and for any underdoped δ ($\lesssim 0.15$), the AF order arises for $J/t = 0.3$ similarly to the Hubbard model. In contrast with the Hubbard model, however, the d-SC order also arises down to small δ in a wide range of t'/t ($\gtrsim -0.2$), and coexists with the AF order even for $t'/t < 0$ (type-II AF regime). Furthermore, there is no instability toward PS for any t'/t and δ for $J/t = 0.3$.

1. Introduction

In cuprate superconductors (SCs),[1] the antiferromagnetic (AF) orders in the insulating parent compounds rapidly vanish on carrier doping and the $d_{x^2-y^2}$-wave superconducting (d-SC) orders arise in wide ranges of doping rate (δ).[2] Formerly, many theoretical studies supported this fundamental feature as well as other properties of $d_{x^2-y^2}$-wave superconductivity (d-SC) on the basis of Hubbard-type or t-J-type models.[3–12] However, recent numerical studies on square-lattice Hubbard (t-t'-U) models using refined techniques which simultaneously consider the two orders[13–15] argued that AF long-range orders prevail in wide ranges of δ and t'/t (diagonal hopping) or phase separation (PS) occurs for $t' \sim 0$, and as a result, the ranges where pure d-SC orders appear are limited to narrow windows in the overdoped regime.

In a previous study,[16] applying a variational Monte Carlo (VMC) method to a strongly correlated Hubbard (t-t'-U) model, we obtained basically the same results: A band-renormalization effect (BRE) plays an essential role for the stabilization of AF orders for large values of $|t'/t|$ through retrieving the nesting. Consequently, states with AF orders or PS become remarkably more stable than a pure d-SC state in the whole underdoped regime and the whole realistic range of t'/t (Fig. 27 in Ref. 16). This result is serious in that it is obtained using a variation theory, which gives an upper bound of the exact energy. Namely, for realizing a pure d-SC order, breakthrough improvement is required in the trial d-SC states, notwithstanding such d-SC states already properly describe various aspects of cuprate SCs as mentioned above. It is important to check whether this perplexing feature is characteristic of the Hubbard model.

In this context, it is significant to study the same subjects in the t-J model,[17] another key model of cuprates. The t-J model possibly has aspects different from the Hubbard model for realistic values of J/t ($\sim 0.2 - 0.5$), although the two models are connected for J/t (t/U) $\rightarrow 0$ and $\delta \sim 0$.[18–20] In the studies of pure (single-order AF and d-SC) states,[5–8] it has

been known that the d-SC order is predominant and overcomes antiferromagnetism (AF) even for very small doping rates. Furthermore, the domain of d-SC extends up to sizable doping rates $\delta \sim 0.5$ for negative large values of t'/t with a moderate J/t.[21–25] The t-J model seems to have a somewhat stronger tendency toward d-SC than the Hubbard model.

Because the t-J model works in the strong-correlation limit, methods applicable to the present subject beyond mean-field levels are restricted. Among others, the VMC method[26] has a crucial advantage, namely, it can treat correlation factors exactly, including the local constraint of no double occupancy, with sufficiently large systems. Thus, this method has been often applied to the problems of (a) coexistence and exclusivity of the two orders and of (b) instability toward PS.[27–33] However, the conclusions of (a) and (b) were not necessarily unified among the studies but seemed rather scattered. Furthermore, the physics underlying them has not been clarified. The previous paper,[16] addressing this subject in the Hubbard model, showed that vital to these problems is the value of t'/t, whose importance had been often disregarded. Here, we will carry out a similar analysis for the t-J model.

In Table I, we summarize the conclusions as to the above two problems of relevant VMC studies for the t-J model and of recent ones for the Hubbard model. We add a result of the extended Gutzwiller approximation[34] as a representative of analytic calculations that respect the local constraint. The conclusions are classified according to $t'/t = 0$ or ~ -0.3 (typical values of hole-doped cuprates). For the simple square lattice ($t'/t = 0$), all studies unanimously showed the coexistence of the two orders, and the values of the critical doping rate δ_{AF} are broadly similar. This feature is also common to that of the Hubbard model. However, the t-J model with $J/t \sim 0.3$ has stability against PS, in contrast with the Hubbard model with $U/t = 12$. On the other hand for $t'/t \sim -0.3$, the conclusions as to whether the two orders coexist or not and the values of δ_{AF} largely depend on the studies. This dependence seems to result from whether the band renormalization (BR) is properly introduced or not.

In this paper, we study the interplay of AF and d-SC or-

Table I. Results of interplay between the AF and d-SC orders in mixed states are compared among relevant VMC (and extended Gutzwiller approximation) studies for the square-lattice t-J model and recent VMC studies for the Hubbard model (lowest three). The upper row of the second column shows whether (or how) BR is introduced. The total number of BR parameters, if known, is entered in brackets. The lower row indicates a typical value of J/t (or U/t) studied. The upper row of the third and fourth columns indicates whether the state is coexistent or exclusive (with realized order). The lower row indicates whether the realized state is homogeneous or phase separated, and the value of δ_{AF}, above which the AF orders vanish, is shown in brackets. For $\delta > \delta_{\mathrm{AF}}$, d-SC appears for all cases shown here.

Literature (Method, Year)	BR (J/t, U/t)	$t'/t = 0$ (δ_{AF})	$t'/t \sim -0.3$ (δ_{AF})
Ref. 34 (Ext.GA, '03)	No (0.3)	Coexistent — (~ 0.11)	—
Ref. 29 (VMC, '99)	No (0.3)	Coexistent Homo. (~ 0.1)	—
Ref. 30 (VMC, '04)	No (1/3)	Coexistent PS (~ 0.1)	—
Ref. 31 (VMC, '04)	Partially (0.3)	Coexistent — (~ 0.1)	Exclusive, AF — (~ 0.06)
Refs. 22, 32 (VMC, '06,'08)	No (0.2)	Coexistent Homo. (~ 0.12)	Coexistent — (~ 0.1)
Ref. 24 (VMC, '09)	No (0.3)	—	Coexistent — (~ 0.1)
Ref. 25 (VMC, '16)	Partially (4) (0.3)	—	Coexistent Homo. (~ 0.08)
This work (VMC, '18)	Yes (8) (0.3)	Coexistent Homo. (~ 0.14)	Exclusive, AF Homo. (~ 0.20)
Ref. 35 (VMC, '16)	No (10)	Coexistent PS, Homo. (~ 0.12)	—
Ref. 14 (m-VMC, '14)	Implicitly (10)	Coexistent PS (~ 0.18)	Exclusive, AF Homo. (~ 0.24)
Ref. 16 (VMC, '16)	Yes (8) (12)	Coexistent PS (~ 0.15)	Exclusive, AF Homo. (~ 0.25)

ders in the t-t'-J model by comparing pure (AF and d-SC) states and a mixed state of the two orders, in the framework of VMC. Into the trial states, we introduce BR parameters independently for the AF and d-SC parts. We also take account of nearest-neighbor correlation factors which distinguish all patterns of bond configurations. In this way, we clarify the following points: (i) How the pure AF state is stabilized by BRE and exhibits a kind of Lifshitz transition in which the loci of pocket Fermi surfaces (FSs) switch, as seen in the Hubbard model.[16] (ii) How BRE affects the pure d-SC state. (iii) How the property of coexistence or exclusivity of the two orders evolves as t'/t and δ are varied in the mixed state. And, we will trace the cause of this property by comparing the behavior between the pure states and mixed state. (iv) Whether or not the states are stable against PS. As a summary, we construct a phase diagram in t'-δ plane using the mixed state (Fig. 21), in order to compare with that for the Hubbard model.

This paper is organized as follows: In Sect. 2, we explain the model and method used. In Sect. 3, we discuss BRE on the pure AF and d-SC states. In Sect. 4, we study the interplay of the two orders using the mixed state. In Sect. 5, we recapitulate this work. In Appendix A, we describe the details of optimizing the trial wave functions. In Appendix B, we argue that the energy reduction in the AF state is primarily caused by FS renormalization but not by the band form. Preliminary results of the present study were published in a conference proceedings.[36]
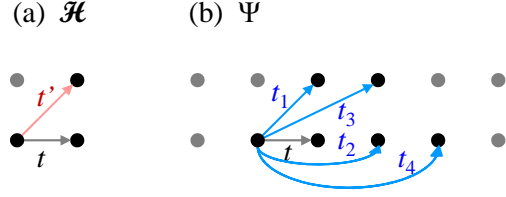

Fig. 1. (Color online) (a) Hopping processes in Hamiltonian [Eq. (2)] and (b) those corresponding to band-adjusting parameters t_η ($\eta = 1 - 4$) in trial wave functions [Eqs. (12) and (18) – (21)]. In both panels, t is the unit.

2. Formulation

After introducing the model Hamiltonian in Sect. 2.1, we explain the VMC method, especially, the trial wave functions in Sect. 2.2. Relevant quantities are defined in Sect. 2.3.

2.1 t-t'-J model

We consider the t-J model on the square lattice[17] with a diagonal transfer term [Fig. 1(a)]

$$\mathcal{H} = \mathcal{H}_{\mathrm{hop}} + \mathcal{H}_J = \mathcal{H}_t + \mathcal{H}_{t'} + \mathcal{H}_J \qquad (1)$$

$$= -t \sum_{\langle i,j \rangle, \sigma} \left(\tilde{c}_{i\sigma}^\dagger \tilde{c}_{j\sigma} + \mathrm{H.c.} \right) - t' \sum_{(i,j), \sigma} \left(\tilde{c}_{i\sigma}^\dagger \tilde{c}_{j\sigma} + \mathrm{H.c.} \right) \qquad (2)$$

$$+ J \sum_{\langle i,j \rangle} \left(\mathbf{S}_i \cdot \mathbf{S}_j - \frac{1}{4} \tilde{n}_i \tilde{n}_j \right), \qquad (3)$$

where $\tilde{c}_{j\sigma} = c_{j\sigma}(1 - n_{j-\sigma})$ is the annihilation operator that acts in the space without double occupation, $c_{j\sigma}$ is the ordinary annihilation operator for the Wannier state, $\tilde{n}_{j\sigma} = \tilde{c}_{j\sigma}^\dagger \tilde{c}_{j\sigma}$, and $\mathbf{S}_j = \frac{1}{2} \sum_{\alpha,\beta} c_{j\alpha}^\dagger \sigma_{\alpha\beta} c_{j\beta}$ (σ : Pauli matrix). $\langle i, j \rangle$ and (i, j) in the summations in Eqs. (2) and (3) indicate the pairs of nearest-neighbor and diagonal-neighbor sites, respectively. Thus, the bare band dispersion is

$$\tilde{\varepsilon}_{\mathbf{k}} = -2t \left(\cos k_x + \cos k_y \right) - 4t' \cos k_x \cos k_y. \qquad (4)$$

The value of t'/t depends on the kind of cuprate SCs and is considered -0.1 (LSCO) $- -0.3$ (YBCO,BSCCO) for hole-doped systems and ~ 0.3 for electron-doped systems (through electron-hole transformation).[37] According to band calculations,[38,39] the existence of apical oxygen tends to increase t'/t. We repeat that the value of t'/t plays a leading role in the present subject. As for J/t, we mainly discuss a typical case for cuprates $J/t = 0.3$, although we sometimes refer to J/t dependence. The Hamiltonian Eq. (1) is connected to the Hubbard Hamiltonian through the strong-coupling expansion for J/t, $t/U \to 0$ with $J = 4t^2/U$ near half filling.[18] Thereby, $J/t = 0.3$ corresponds to $U/t = 13.3$. We use t and the lattice spacing as the units of energy and length, respectively.

2.2 Variational Monte Carlo method

A merit of the VMC method[26] is the possibility of specifying important factors or physics (e.g. BRE) in the system of our interest. To this end, it is vital to construct simple trial wave functions that capture the essence. In this study, as many-body trial states, we use a Jastrow type, $\Psi = \mathcal{P}\Phi$,[40] where $\mathcal{P}$ is a two-body correlation factor (projector) and Φ is

a one-body (mean-field-type) wave function.

We take the form of $\mathcal{P}$ common to all trial states, $\mathcal{P} = \mathcal{P}_G \mathcal{P}_J$. Here, $\mathcal{P}_G$ is the onsite projector $\mathcal{P}_G = \prod_j [1 - n_{j\uparrow} n_{j\downarrow}]$[41] that ensures the above local constraint. In the intersite factor $\mathcal{P}_J$, we consider both charge-density and spin correlations between nearest-neighbor sites: $\mathcal{P}_J = \mathcal{P}_h \mathcal{P}_S$. For the charge-density part, we use an interhole correlation,

$$\mathcal{P}_h = \prod_{\langle i,j \rangle} \left[1 - (1 - \alpha) h_i h_j \right] \tag{5}$$

with $h_j = (1 - \tilde{n}_{j\uparrow})(1 - \tilde{n}_{j\downarrow})$. For the spin-dependent part, we use the form,

$$\mathcal{P}_s = \prod_{\langle i,j \rangle} \left[1 - (1 - \beta_1)(\tilde{n}_{i\uparrow}\tilde{n}_{j\uparrow} + \tilde{n}_{i\downarrow}\tilde{n}_{j\downarrow}) \right]$$
$$\times \left[1 - (1 - \beta_2)(\tilde{n}_{i\uparrow}\tilde{n}_{j\downarrow} + \tilde{n}_{i\downarrow}\tilde{n}_{j\uparrow}) \right]. \tag{6}$$

In Eqs. (5) and (6), α, β_1 and β_2 are variational parameters. $\mathcal{P}_h$ is effective, especially, in a highly doped regime. $\mathcal{P}_s$ plays a corrective role for the (often overestimated) AF order. Using $\mathcal{P}_h$ and $\mathcal{P}_s$, we can assign distinct weights to all different nearest-neighbor bond configurations.

We turn to the one-body part Φ, into which BRE[33,42] is introduced. The forms used in the previous study[16] are applied to the present cases. We start with the normal (paramagnetic) state (Fermi Sea),

$$\Phi_N = \prod_{\{k\}_{occ}, \sigma} c^\dagger_{k,\sigma} |0\rangle, \tag{7}$$

where $\{k\}_{occ}$ indicates the set of occupied wave-number points of $k \in k_F$. Although there is no explicit variational parameter in Φ_N, we have to determine $\{k\}_{occ}$ variationally as in the AF case when BRE is considered (see below and Appendix A).

For the (commensurate) AF state, we apply the form of Hartree-Fock (HF) solution for $t' = 0$ at half filling, in which case the nesting condition is completely satisfied, to the other cases of t'/t and δ in a sense of variation theory:

$$\Phi_{AF} = \prod_{\{k\}_{occ}, \sigma} a^\dagger_{k,\sigma} |0\rangle, \tag{8}$$

where, $a^\dagger_{k,\sigma}$ is an AF quasiparticle operator given as

$$a^\dagger_{k,\sigma} = \alpha_k c^\dagger_{k,\sigma} + \text{sgn}(\sigma)\, \beta_k c^\dagger_{k+Q,\sigma}, \tag{9}$$

$$a^\dagger_{k+Q,\sigma} = -\text{sgn}(\sigma)\, \beta_k c^\dagger_{k,\sigma} + \alpha_k c^\dagger_{k+Q,\sigma}. \tag{10}$$

In Eqs. (9) and (10), k is taken in the folded AF Brillouin zone with the lower-band energy dispersion,

$$E^{AF}_k = \frac{U}{2} - \sqrt{\gamma_k^2 + \Delta_{AF}^2}, \tag{11}$$

$$\gamma_k = -2t(\cos k_x + \cos k_y), \tag{12}$$

$Q = (\pi, \pi)$, $\text{sgn}(\sigma) = 1 \,(-1)$ for $\sigma = \uparrow (\downarrow)$, and

$$\alpha_k\,(\beta_k) = \frac{1}{\sqrt{2}} \sqrt{1 - (+)\frac{\varepsilon^{AF}_k}{\sqrt{\left(\varepsilon^{AF}_k\right)^2 + \Delta_{AF}^2}}}. \tag{13}$$

Δ_{AF} corresponds to the AF gap in the sense of HF theory.[43] In Eq. (13), allowing for BRE (explained shortly), we write ε^{AF}_k for the energy dispersion, instead of γ_k. The choice of $\{k\}_{occ}$, namely FS, is included in the BR processes of Ψ_N, Ψ_{AF} and Ψ_{mix}, and is not easy operation for finite-size systems.[11] We

Table II. Comparison of form of ε^Λ_k and choice of $\{k\}_{occ}$ for band renormalization in mixed states among related studies. The second column (d-SC) shows the energy dispersion to be optimized in the one-body d-SC part and the third column (AF) the same but in the AF part. In the fourth column, the total number of band parameters are entered. The rightmost column indicates how to choose the occupied k-points in the AF part.

Literature	d-SC	AF	Param.	$\{k\}_{occ}$ in AF part
Ref. 33	ε^{SC}_k	γ_k	4	Order of γ_k
Ref. 25	ε^{SC}_k	$\varepsilon^{AF}_k \equiv \varepsilon^{SC}_k$	4	Order of γ_k
Ref. 16	ε^{SC}_k	ε^{AF}_k	8	Order of ε^{AF}_k
Present work	ε^{SC}_k	ε^{AF}_k	8	Optimizing Ψ_{mix}

describe, in Appendix A, how we deal with the optimization of $\{k\}_{occ}$ in this study. Φ_{AF} is reduced to Φ_N for $\Delta_{AF} = 0$.

The pure $d_{x^2-y^2}$-wave singlet pairing (BCS) state of a fixed electron number N is given by[44]

$$\Phi_d = \left(\sum_k \phi(k)\, c^\dagger_{k\uparrow} c^\dagger_{-k\downarrow} \right)^{\frac{N}{2}} |0\rangle, \tag{14}$$

where

$$\phi(k) = \frac{\Delta_k}{\varepsilon^{SC}_k - \mu + \sqrt{(\varepsilon^{SC}_k - \mu)^2 + \Delta_k^2}}, \tag{15}$$

with $\Delta_k = \Delta_d(\cos k_x - \cos k_y)$. Δ_d and μ are variational parameters corresponding to the d-SC gap and chemical potential. In ε^{SC}_k, BRE is introduced. Φ_d is reduced to Φ_N for $\Delta_d = 0$ and $\mu = \mu_0$ (μ_0: the non-interacting chemical potential).

The mixed state, which can simultaneously have d-SC and AF orders,[27–29] are constructed by replacing the bare electron operator $c^\dagger_{k,\sigma}$ in Eq. (14) by the AF quasiparticle operator $a^\dagger_{k,\sigma}$ in Eqs. (9) and (10) as[28]

$$\Phi_{mix} = \left(\sum_k \phi(k)\, a^\dagger_{k\uparrow} a^\dagger_{-k\downarrow} \right)^{\frac{N}{2}} |0\rangle. \tag{16}$$

Φ_{mix} is reduced to the pure states in certain limits, namely, Φ_d for $\Delta_{AF} = 0$ and Φ_{AF} for $\Delta_d = 0$ and $\mu = \mu_0$.

For introducing BRE into Φ_{AF}, Φ_d and Φ_{mix}, we extend the band dispersions ε^{AF}_k in Eq. (13) and ε^{SC}_k in Eq. (15) by including tight-binding hopping terms up to three-step processes shown in Fig. 1(b) as,

$$\varepsilon^\Lambda_k = \gamma_k + \varepsilon^\Lambda_1(k) + \varepsilon^\Lambda_2(k) + \varepsilon^\Lambda_3(k) + \varepsilon^\Lambda_4(k), \tag{17}$$

with $\Lambda = $ SC or AF and

$$\varepsilon^\Lambda_1(k) = -4t^\Lambda_1 \cos k_x \cos k_y, \tag{18}$$

$$\varepsilon^\Lambda_2(k) = -2t^\Lambda_2(\cos 2k_x + \cos 2k_y), \tag{19}$$

$$\varepsilon^\Lambda_3(k) = -4t^\Lambda_3(\cos 2k_x \cos k_y + \cos k_x \cos 2k_y), \tag{20}$$

$$\varepsilon^\Lambda_4(k) = -2t^\Lambda_4(\cos 3k_x + \cos 3k_y). \tag{21}$$

These band-adjusting (variational) parameters t^Λ_η/t ($\eta = 1$–4) are independent of the model parameter t'/t in $\mathcal{H}$ and of t_p/t used for determining $\{k\}_{occ}$ (see Appendix A). Thus, we have four band parameters in Φ_{AF} and Φ_d, and eight in Φ_{mix}. In Φ_{mix}, it is crucial to optimize t^{SC}_η and t^{AF}_η, independently. Actually, for the Hubbard model,[16] only t^{SC}_1/t is effective in the d-SC part, but t^{AF}_η/t up to $\eta = 4$ become important for the nesting in the AF part. Furthermore, there is room for how to choose $\{k\}_{occ}$ in the AF part. In Table II, we compare the ways

of introducing BRE into mixed states among related studies. In this work (the last row), we take t_η^{AF}/t and t_η^{SC}/t as eight independent band parameters, and determine $\{\mathbf{k}\}_{\mathrm{occ}}$ so as to minimize the total energy with respect to Ψ_{mix}, instead of using some guiding energy dispersion. Therefore, the present way of introducing BRE comprehends the other ways in Table II as special cases. The independence of t_η^{AF}/t and t_η^{SC}/t is, in particular, important; otherwise, qualitatively different results are sometimes derived,[25,33] as shown in Table I above and Table IV in Ref. 16. We describe the details of optimizing $\{\mathbf{k}\}_{\mathrm{occ}}$ in this work in Appendix A.

Variational expectation values of $\hat{O}$ with respect to Ψ_Λ ($= \mathcal{P}\Phi_\Lambda$; $\Lambda = $ N, AF, d, and mix),

$$\langle \hat{O} \rangle_\Lambda = \frac{\langle \Psi_\Lambda | \hat{O} | \Psi_\Lambda \rangle}{\langle \Psi_\Lambda | \Psi_\Lambda \rangle} \quad (22)$$

are numerically estimated using a VMC method[26] for finite systems of $N_{\mathrm{s}} = L \times L$ sites ($L = 10 - 24$) with the periodic-antiperiodic boundary conditions. The number of samples for computing $\langle \hat{O} \rangle$ are typically 2.5×10^5. Optimization of the variational parameters except for t_{p}/t (see Appendix) is performed using the stochastic reconfiguration method.[45]

2.3 Physical quantities

Here, we define quantities often referred to. The total energy per site of the state Λ is written as $E_\Lambda = \langle \mathcal{H} \rangle_\Lambda / N_{\mathrm{s}}$. As the AF order parameter, staggered magnetization,

$$m = \frac{2}{N_{\mathrm{s}}} \sum_j \left| e^{i\mathbf{Q}\cdot\mathbf{r}_j} \langle S_j^z \rangle \right|, \quad (23)$$

is used, where $\mathbf{Q}$ is the AF nesting vector (π, π). m becomes unity for the full moment. As the indicator of d-SC order, we use the real-space d-SC correlation function for the nearest-neighbor-site pairing, $P_d \equiv P_d(\mathbf{r}_\infty)$ with $\mathbf{r}_\infty = (L/2, L/2)$ and

$$P_d(\mathbf{r}) = \frac{1}{N_{\mathrm{s}}} \sum_i \sum_{\tau,\tau'=\hat{x},\hat{y}} (-1)^{1-\delta(\tau,\tau')} \left\langle \Delta_\tau^\dagger(\mathbf{R}_i) \Delta_{\tau'}(\mathbf{R}_i + \mathbf{r}) \right\rangle, \quad (24)$$

where $\hat{x}$ ($\hat{y}$) denotes the lattice vector in x (y) direction, $\delta(\tau, \tau')$ indicates the Kronecker delta, and $\Delta_\tau^\dagger(\mathbf{R}_i)$ is the creation operator of a nearest-neighbor singlet pair at site $\mathbf{R}_i$,

$$\Delta_\tau^\dagger(\mathbf{R}_i) = (c_{i\uparrow}^\dagger c_{i+\tau\downarrow}^\dagger + c_{i+\tau\uparrow}^\dagger c_{i\downarrow}^\dagger)/\sqrt{2}. \quad (25)$$

To evaluate the contribution of AF correlation, we display the $\mathbf{q} = \mathbf{Q}$ element of the spin structure factor,

$$S(\mathbf{q}) = \frac{1}{N_{\mathrm{s}}} \sum_{ij} e^{i\mathbf{q}\cdot(\mathbf{R}_i - \mathbf{R}_j)} \left\langle S_i^z S_j^z \right\rangle. \quad (26)$$

For studying the electronic state, we use the momentum distribution function,

$$n(\mathbf{k}) = \frac{1}{2} \sum_\sigma \langle c_{\mathbf{k}\sigma}^\dagger c_{\mathbf{k}\sigma} \rangle, \quad (27)$$

in which available $\mathbf{k}$ points are shifted by π/L in y direction owing to the boundary conditions used.

3. Results of Pure States

In Sects. 3.1 and 3.2, we discuss noteworthy aspects of the pure d-SC state Ψ_d and pure AF state Ψ_{AF}, respectively.
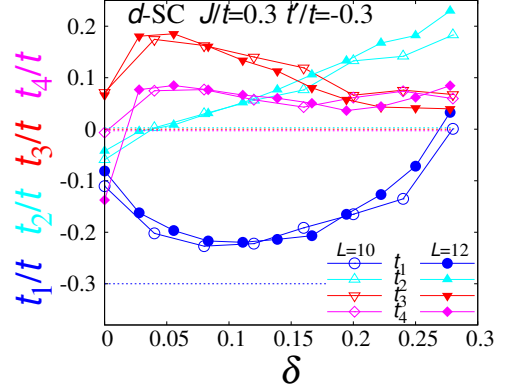

Fig. 2. (Color online) The optimized band parameters $t_\eta^{\mathrm{SC}} \equiv t_\eta$ ($\eta = 1$–4) in Ψ_d are depicted as a function of doping rate for $t'/t = -0.3$. The values of t_η without BR are indicated by dotted lines in coordinate colors.

Table III. Energy improvement owing to band renormalization $\Delta E_\Lambda^{\mathrm{BR}}/t$ ($\Lambda =$ AF, SC) [Eq. (28)] in the pure states for three typical values of t'/t and doping rate. $J/t = 0.3$ and $L = 10$. For comparison, we show the corresponding data of the Hubbard model with $U/t = 12$ borrowed from Ref. 16. The last digit of each has some error.

States	$t'/t \setminus \delta$	0.0	0.08	0.16
d-SC	-0.3	0.0009	0.0017	0.0038
	0.0	0.0001	0.0002	0.0005
	$+0.3$	0.0009	0.0001	0.0001
AF	-0.3	0.0601	0.0405	0.0251
	0.0	0.0001	0.0009	0.0010
	$+0.3$	0.0586	0.0307	0.0087
d-SC (Hubbrad)	-0.3	0.0019	0.0004	0.0001
	0.0	0.0000	0.0002	0.0005
	$+0.3$	0.0001	0.0003	0.0005
AF (Hubbrad)	-0.3	0.1653	0.0622	0.0220
	0.0	0.0058	0.0102	0.0020
	$+0.3$	0.1653	0.0603	0.0108

3.1 d-wave superconducting state

In a previous study[16] for the Hubbard model, it was found that BRE in Ψ_d affects only very slightly physical quantities as well as energy for large U/t and $|t'/t|$, compared to Ψ_{AF}, although the renormalization of t_1^{SC}/t in Ψ_d is never small.[21,23,46] In Fig. 2, we plot δ dependence of the optimized band parameters of the d-SC states for the t-J model with $t'/t = -0.3$. For $\delta \sim 0$ and in the overdoped regime ($\delta \gtrsim 0.16$), t_1/t is greatly renormalized, namely, going away from -0.3; the large BR in the latter regime is absent in the Hubbard model (See Fig. 3 in Ref. 16). Since t_2/t linearly increases with δ, BR becomes large (t_2/t goes away from 0) in the overdoped regime. This behavior contrasts with that for the Hubbard model, where t_2/t substantially vanishes for any δ. For $t'/t = 0.3$ (not shown), more marked BR exists in t_1/t ($-0.1 \lesssim t_1/t \lesssim 0.1$) for $\delta \lesssim 0.2$, and $t_2/t \sim -0.05$ for most δ. Thus, the renormalization of t_1/t and t_2/t becomes appreciable in Ψ_d for the t-J model.

In Table III, we show the energy improvement owing to BRE for the t-J model:

$$\Delta E_\Lambda^{\mathrm{BR}} = E_\Lambda(\text{no BR}) - E_\Lambda, \quad (28)$$

where $E_\Lambda(\text{no BR})$ is the energy per site of the state Λ [$\Lambda =$ AF or d] calculated without BR, namely, using the band parameters t_η^Λ (and t_{p} for AF) fixed at the values in $\mathcal{H}$. Notable features are found in $\Delta E_\Lambda^{\mathrm{BR}}$: (i) Both for the d-SC and AF
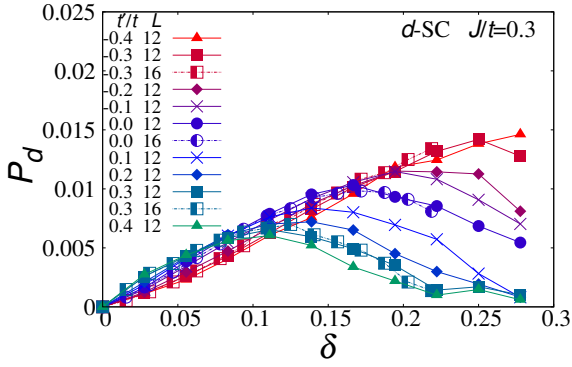
Fig. 3. (Color online) Doping rate dependence of d-wave SC correlation function P_d calculated using Ψ_d for various values of t'/t (and L).
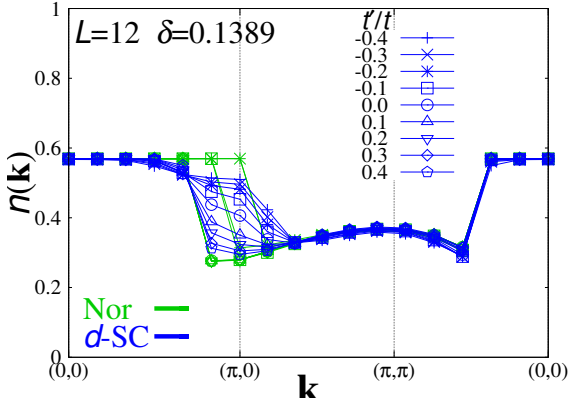

Fig. 4. (Color online) The momentum distribution function of the pure d-SC state is drawn along the path of $\mathbf{k}$: $(0,0)$-$(\pi,0)$-(π,π)-$(0,0)$. Results for various values of t'/t are drawn in blue. For comparison, corresponding results of the normal (paramagnetic) state are added in green. $J/t = 0.3$.
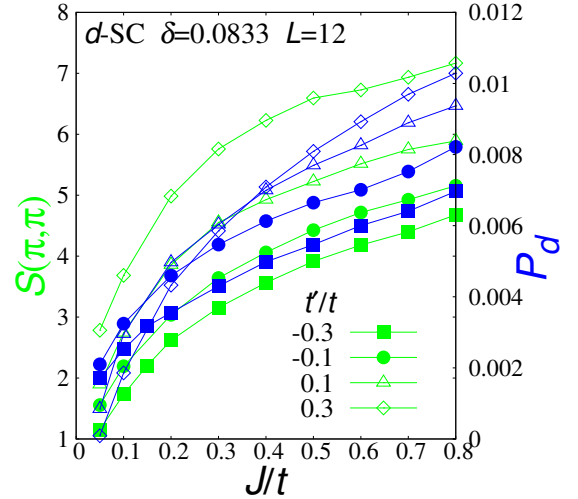

Fig. 5. (Color online) J/t dependence of the spin correlation function at $\mathbf{q} = (\pi, \pi)$ (green) and the d-SC correlation function (blue) calculated using Ψ_d are compared for four t'/t. The figures of the symbols are common to $S(\mathbf{q})$ and P_d.
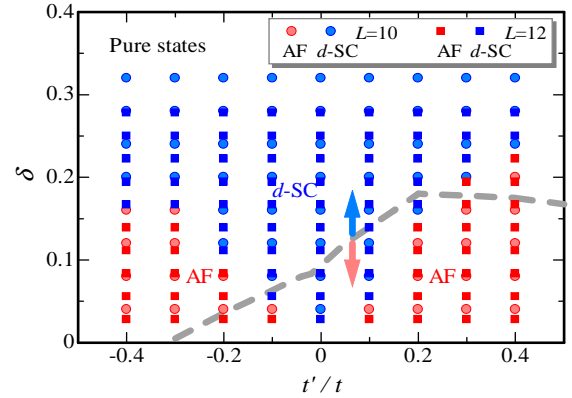

Fig. 6. (Color online) t'-δ phase diagram constructed by comparing energies of pure AF and d-SC states. For large $|t'/t|$, the AF domain is likely to expand to the large-δ direction for technical reasons.[48] The bold gray dashed line indicate a similar AF-d-SC boundary determined using the data without BR for the Hubbard model of $U/t = 12$.[11,16] The difference of models does not affect the aspect for large $|t'/t|$.

states, BRE is almost ineffective for $t'/t = 0$. (ii) Energy improvement in the d-SC state is small for any t'/t and δ, despite the above large BR in t_1/t and t_2/t. (iii) Energy improvement in the AF state is one or two orders of magnitude larger than in the d-SC state for $t'/t = \pm 0.3$. These features of the t-J model is common to those of the Hubbard model.[16] Owing to the feature (i), the results of previous studies for $t'/t = 0$ in Table I are almost identical despite whether BRE is introduced or not. The feature (ii) indicates that various properties of Ψ_d are almost unchanging by BRE. The feature (iii) will be discussed later in Sect. 3.2. These features are identical with those of the Hubbard model.

We notice in Table III that δ dependence of ΔE_d^{BR} is opposite between the t-J and Hubbard models for $t'/t = -0.3$, although its magnitude is not large. This feature stems from the above contrastive behavior of t_1 and t_2, and is probably related to the prevalence of d-SC order for large negative t'/t in the t-J model.[21–25] This prevalence is confirmed by P_d [Eq. (24)] shown in Fig. 3 and is hardly changed by BRE; the range of d-SC seems very wide (probably up to $\delta = 0.5$), as compared to the Hubbard model.[11] The dome-like δ dependence of d-SC correlation has been well-known since early studies of the t-J model.[6]

Shown in Fig. 4 is $n(\mathbf{k})$ for various values of t'/t. As a feature of $d_{x^2-y^2}$-wave symmetry, a Fermi point exists in the nodal direction near $(\pi/2, \pi/2)$,[9] whereas a gap opens near the antinodal $(\pi, 0)$ in contrast with the case of Ψ_N. Note that, as t'/t is varied, the behavior near the antinodal markedly changes, but is almost unchanging for the other $\mathbf{k}$. Because the property of d-SC appreciably changes with t'/t as shown in Fig. 3,

the electrons with $\mathbf{k}$ near antinodal must play a leading role for d-SC.[16] This feature is common to that of the Hubbard model.[11]

We turn to the relation between the d-SC order and AF correlation. In Fig. 5, we plot P_d and $S(\mathbf{q})$ [Eq. (26)] with $\mathbf{q} = \mathbf{Q} = (\pi, \pi)$ as a function of J/t. As the spin exchange interaction J/t increases, P_d increases faithfully according to $S(\mathbf{Q})$ for any t'/t, meaning that the driving force of d-SC is the AF exchange interaction. Therefore, the scattering process (or a vector connecting FSs) of $\mathbf{Q}$ comes to play a crucial role for raising d-SC.[17,47]

These properties are consistent with the results of previous studies. We will discuss the stability against PS of Ψ_d together with the case of Ψ_{AF} in Sect. 3.2.

3.2 Antiferromagnetic state

As mentioned in Sect. 3.1 [feature (iii)], BRE is highly effective in reducing the energy of the AF state for large $|t'/t|$. This energy reduction is primarily caused by the FS renormalization (choice of $\{\mathbf{k}\}_{\mathrm{occ}}$) but not by the band form $\varepsilon_{\mathbf{k}}^{\mathrm{AF}}$
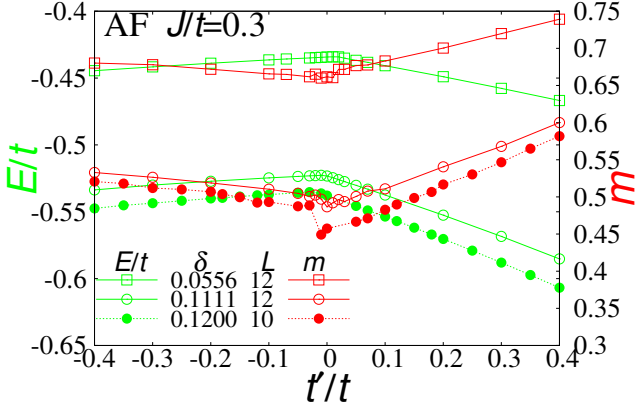
Fig. 7. (Color online) t'/t dependence of total energy per site (green, left axis) and staggered magnetization [Eq. (23)] (red, right axis) of Ψ_{AF}. Three cases of δ (and L) are shown.
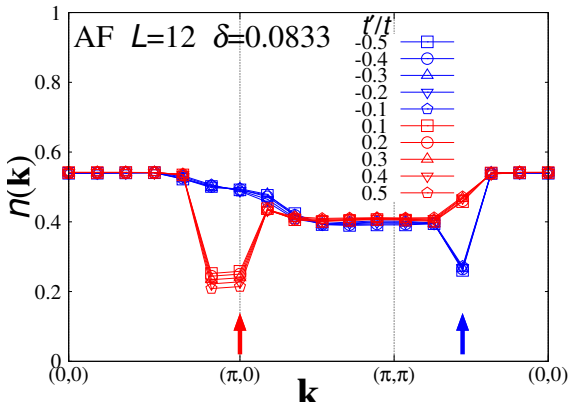

Fig. 8. (Color online) The momentum distribution function calculated using metallic ($\delta > 0$) Ψ_{AF} is shown along the same path as in Fig. 4. The cases of various t'/t are compared. The data of type-I (II) AF state are shown with red (blue) symbols. The Lifshitz point is $t'_L/t \sim 0$. The red (blue) arrow indicates the loci of pocket Fermi surfaces of the type-I (type-II) AF state.

Fig. 9. (Color online) Doping-rate dependence of the momentum distribution function of Ψ_{AF} for $J/t = 0.3$. In (a), we plot the results of typical t'/t values of type-I (red) and type-II (blue) AF states for three values of doping rate. The red (blue) arrow indicates the locus of pocket Fermi surface of type-I (type-II) AF. In (b), we plot the results for $t'/t = 0.3$ (type-I) in a wide range of doping rate up to the PM regime $\delta > \delta_{AF}$ (~ 0.20, pale color). The arrow indicates a Fermi surface appearing for the PM state. Shown in the inset is δ dependence of the staggered magnetization of the same systems.

itself, as explained in Appendix B. The energy improvement owing to BRE ΔE_{AF}^{BR} [Eq. (28)] is one or two orders of magnitude larger than ΔE_d^{BR}, as shown in Table III. Thereby, the t'-δ phase diagram constructed within the the pure states is noticeably changed, as shown in Fig. 6. The bold gray dashed line indicates the boundary between AF and d-SC in the case without BRE for the corresponding Hubbard case. The AF range shrinks and vanishes for large negative t'/t. In contrast, by introducing BRE, the AF range expands as $|t'/t|$ increases especially in the negative-t'/t side.[48] Incidentally, it is known for the t-J model with $t'/t = 0$ that the stable state is rapidly switched from AF to d-SC on carrier doping even without BRE.[8] This feature is unchanging by BRE and contrasts with the Hubbard case (gray line). Anyway, this result with BRE is contrary to the common knowledge that the AF state is rapidly destabilized on doping and the d-SC order appears for hole-doped cases ($t'/t < 0$).

Next, we study the (expected) Lifshitz transition in the metallic (doped) AF states, which corresponds to what was found in the Hubbard model.[16] At half filling, an insulating AF state is realized, because the t-J model is reduced to the Heisenberg antiferromagnet.[49,50] This AF is preserved at least for $|t'/t| \leq 0.5$, because the nesting condition is completely retrieved owing to BRE. When carriers are doped,
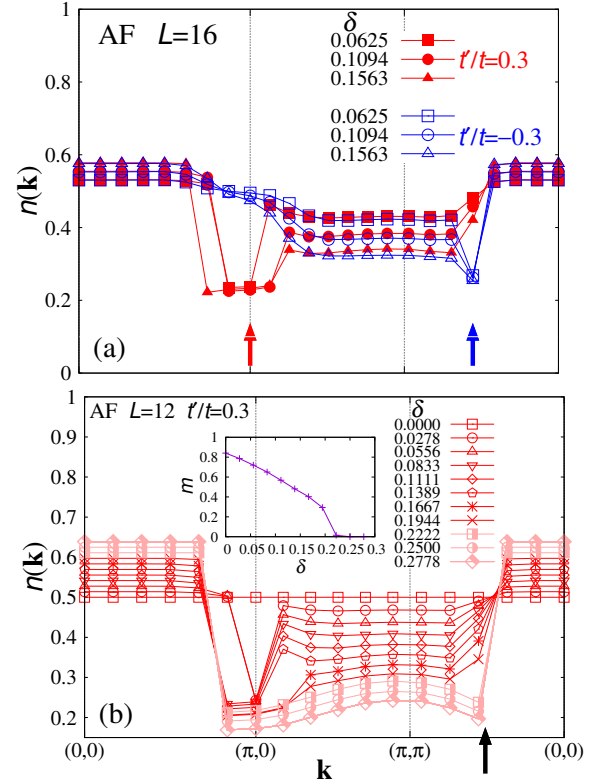
this insulating AF state changes over to metallic with FSs. In Fig. 7, we show t'/t dependence of total energy and staggered magnetization for three doping rates (and L). We find cusps (or small discontinuities in m) in both quantities at $t' = t'_L \sim 0$, suggesting some transition. If this anomaly indicates the aforesaid Lifshitz transition, the loci of the FSs should be switched when t' passes through t'_L. To confirm it, we show, in Fig. 8, the momentum distribution function [Eq. (27)] at $\delta = 0.083$ for various values of t'/t. We find a pocket FS (discontinuity) around $\mathbf{k} = (\pi, 0)$ [$(\pi/2, \pi/2)$] for $t' > t'_L$ [$t' < t'_L$]; the loci of the pocket FS suddenly changes at $t' = t'_L$. This behavior is basically the same as what was found for a strongly correlated Hubbard model.[16] We named the former (latter) state the type-I (type-II) AF state. Related phenomena or behavior in the t-J model as well as the Hubbard model have been studied since the early days of cuprates[51,52] and later in various studies[53] in connection with the difference in ARPES spectra between electron-doped[54] and hole-doped[55] cuprates. Furthermore, this difference greatly affects whether AF and d-SC orders are coexistent or exclusive.[16]

We confirmed that, even if J/t is varied, the above t'/t dependence of $n(\mathbf{k})$ is preserved as far as $J < J_{PS}$, where J_{PS} ($\sim 2.5t$ for $\delta \sim 0.08 - 0.20$) is the transition point to PS (not shown).[56] In Fig. 9, we show the δ dependence of $n(\mathbf{k})$. In (a), we find that the loci of pocket FS are unchanging when δ is varied, regardless of the type of AF, I ($t'/t = 0.3$) or II ($t'/t = -0.3$). Shown in (b) are the data ($t'/t = 0.3$, type-I) for a wider range of δ up to ~ 0.28 in the PM area. The lo-
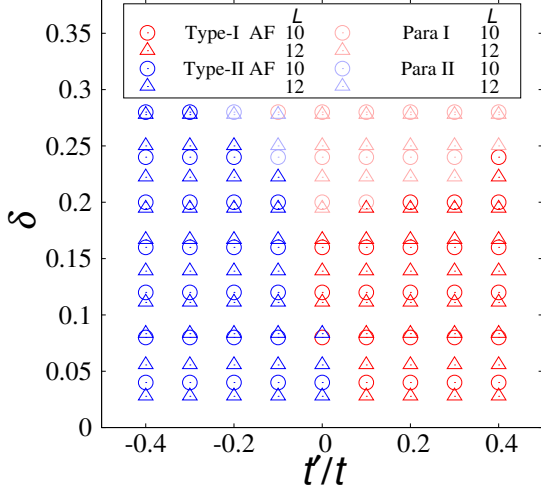
Fig. 10. (Color online) t'-δ diagram according to Fermi-surface topology (occupied **k**-points) in the optimized metallic AF (PM) states. Red circles (triangles) indicate the type-I AF for $L = 10$ ($L = 12$), and similarly blue symbols the type-II AF. The symbols in pale colors indicate the PM cases ($m = 0$), in which the occupied **k**-points are the same as those in the AF states of corresponding types (and L). The boundary between blue and red (dark and pale colors) indicates t_L/t (δ_{AF}).
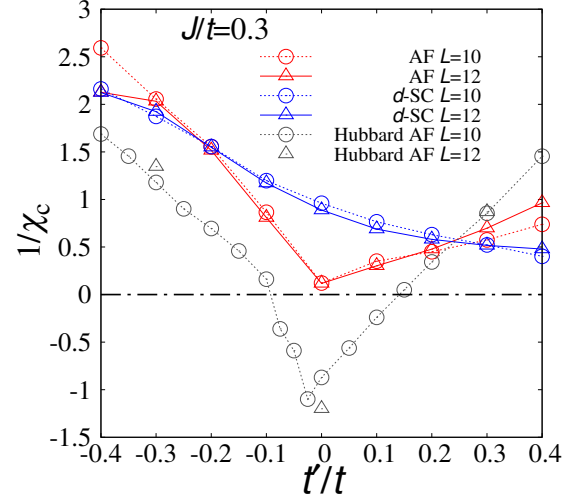

Fig. 11. (Color online) Inverse charge susceptibilities of pure AF (red) and d-SC (blue) states as functions of t'/t. For comparison, the corresponding data of the AF state for the Hubbard model with $U/t = 12$[16] (gray) are added. The horizontal dash-dotted line ($1/\chi_c = 0$) is the boundary of stability against PS.
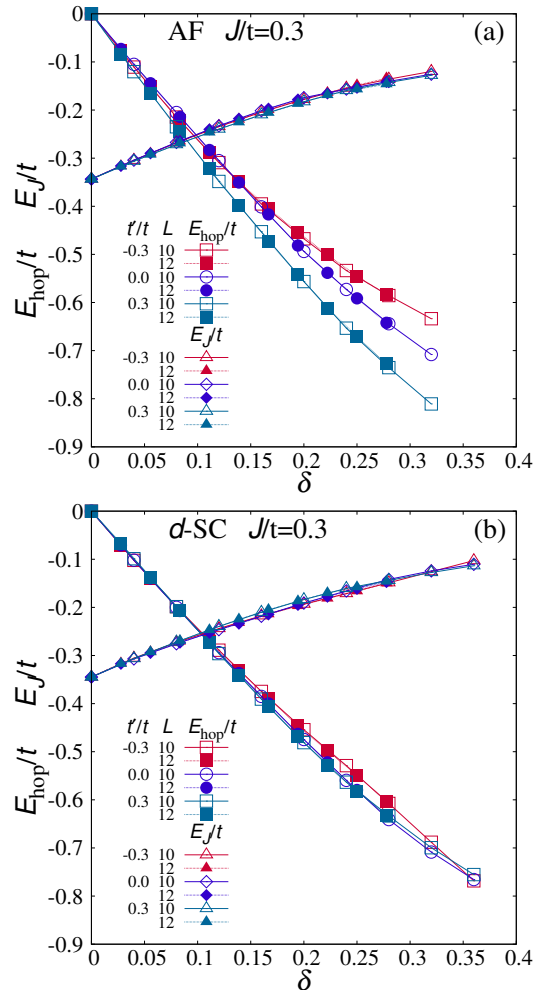
cus of the pocket FS is preserved until the AF order vanishes at $\delta = \delta_{AF} \sim 0.2$ (see m in the inset). The pocket FS of the AF state changes to a global FS centered at $\mathbf{k} = (0, 0)$ of the PM state at $\delta = \delta_{AF}$, but $\{\mathbf{k}\}_{occ}$ is identical between Φ_{AF} and Φ_N. The evolution of $n(\mathbf{k})$ according to δ is similar in type-II cases.

As a summary of FS topology, we construct a diagram of the types of AF order in Ψ_{AF} and of $\{\mathbf{k}\}_{occ}$ in Ψ_N in the t'-δ space (Fig. 10). The Lifshitz point t'_L/t (the boundary between red and blue) slightly shifts to a smaller value as δ increases. Incidentally, in the Hubbard model, the Lifshitz point is situated at $-0.1 < t'_L/t < 0$ for any model-parameter set.[16] Note that the AF order is stable in the whole underdoped regime ($\delta \lesssim 0.16$) for any t'/t.

Finally, we discuss the intrinsic stability against PS of Ψ_{AF}. Following the previous study,[16] we judge this property by the sign of charge susceptibility χ_c,

$$\frac{1}{\chi_c} = \frac{\partial^2 E(\delta)}{\partial \delta^2} = \frac{E(\delta + \Delta\delta) + E(\delta - \Delta\delta) - 2E(\delta)}{(\Delta\delta)^2}. \quad (29)$$

For $\chi_c > 0$ ($\chi_c < 0$), the state is stable against (unstable toward) PS. We found that δ dependence of the energy of Ψ_{AF} is fitted well by the parabolic form

$$E(\delta) \simeq c_0 + c_1\delta + c_2\delta^2, \quad (30)$$

for $\delta < \delta_{AF}$ (except in the $\delta \to 0$ limit). Therefore, we have a unique value $\chi_c = c_2^{-1}$ in the AF phase. In Fig. 11, the values of $1/\chi_c$ thus estimated are plotted in red as a function of t'/t for $L = 10$ and 12. χ_c of Ψ_{AF} for $J/t = 0.3$ is positive for any t'/t, in contrast with that of the Hubbard model with $U/t = 12$ (gray symbols), which becomes negative around $t'/t = 0$. The AF state is always stable against PS for $J/t = 0.3$.

We mention J/t dependence of this property. In Fig. 12(a), we show δ dependence of the two energy elements $E_{hop} = \langle \mathcal{H}_{hop} \rangle / N_s$ and $E_J = \langle \mathcal{H}_J \rangle / N_s$ of Ψ_{AF} for $J/t = 0.3$. For any t'/t, E_{hop}/t is downward-convex and E_J/t is concave; the con-

Fig. 12. (Color online) Doping-rate dependence of two energy elements per site E_{hop} and E_J with respect to pure (a) AF and (b) d-SC states for three typical values of t'/t.
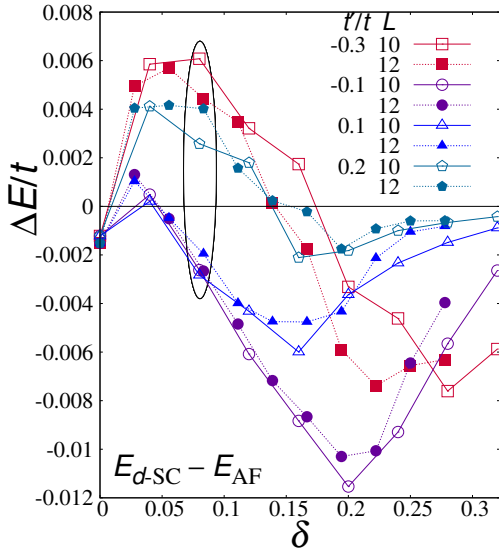
Fig. 13. (Color online) Energy difference between the pure AF and SC states [Eq. (31)] is depicted as a function of doping rate for severa values of t'/t. The zero (black line) is the boundary whether the lower energy is given by Ψ_{AF} or Ψ_d. For positive (negative) $\Delta E/t$, the AF (d-SC) state is more stable. $J/t = 0.3$. The black ring indicates $\delta = 0.08$ used for explanation.

vexity of total energy, namely, stability against PS stems from the hopping energy. Becuase E_J is the factor of instability toward PS, Ψ_{AF} will become unstable as J/t increases and E_J becomes predominant. We would like to address this subject again elsewhere.

At this opportunity, we discuss the stability against PS of other states. In Fig. 11, we also plot $1/\chi_c$ of Ψ_d in blue. Because χ_c is always positive, Ψ_d is stable against PS in the range shown. This property is the same as that in the Hubbard model with $U/t = 12$.[16] In Fig. 12(b), we show δ dependence of the two energy elements. Since both E_{hop} and E_J exhibit a tendency similar to that of Ψ_{AF} in Fig. 12(a), Ψ_d will also phase separates at a large J/t. For the mixed state, we estimate $1/\chi_c$ for each δ for $J/t = 0.3$ using the expression of finite differences in Eq. (29), because the quadratic fit of $E(\delta)$ is deteriorated by the existence of subdivided domains [(1)–(4)], as will be discussed in Sect. 4. Anyway, we find that $1/\chi_c > 0$ holds for any δ (not shown), so that Ψ_{mix} is also stable against PS.

4. Mixed State of AF and d-SC Orders

In this section, we study the interplay of AF and d-SC orders in the mixed state Ψ_{mix}. We start with the energy difference between the two pure states Ψ_{AF} and Ψ_d:

$$\Delta E = E_d - E_{AF}. \tag{31}$$

In Fig. 13, δ dependence of $\Delta E/t$ for $J/t = 0.3$ is shown for various values of t'/t ($L = 10$ and 12). Note that there exist cases in which d-SC is more stable than AF ($\Delta E/t > 0$) in the underdoped regime ($\delta \lesssim 0.16$), in contrast with the Hubbard model with $U/t = 12$.[16] We can divide the δ-t' space into four domains (categories) according to

(1) E_{AF} (type-I) $< E_d$
(2) E_{AF} (type-II) $< E_d$
(3) $E_d < E_{AF}$ (type-I)
(4) $E_d < E_{AF}$ (type-II)

when the AF and/or d-SC orders arise. This classification is convenient to understand the behavior of coexistence or ex-
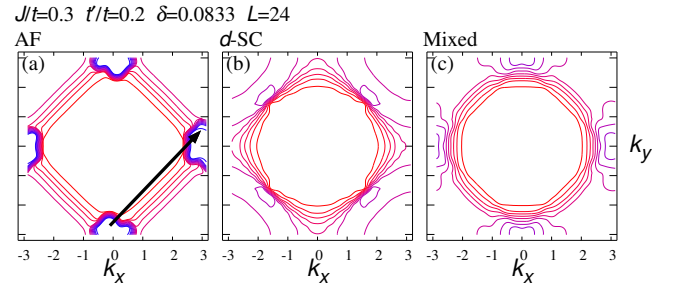
clusivity of the two orders in Ψ_{mix}. Let us focus on the cases of $\delta = 0.08$, because all the above categories (1)–(4) appear.

First, we check whether the two orders coexist or not in each category. In Fig. 14(a), we depict δ dependence of P_d and m calculated using the pure state Ψ_d and Ψ_{AF}, respectively. Shown in Fig. 14(b) are the same quantities simultaneously calculated using the mixed state Ψ_{mix}. In (a), both P_d and m at $\delta = 0.08$ (marked with a ring) are finite for any t'/t, indicating that each order can arise as a single order for any t'/t if the counter order does not arise. And the values of both P_d and m are almost constant with respect to t'/t. In (b), however, P_d vanishes for $t'/t = -0.3$ with m almost unchanging, whereas P_d is almost unchanging for other values of t'/t but m tends to be suppressed, especially, for $t'/t = -0.1$. Thus, we find that in the regime of type-II AF [$t'/t \lesssim 0$, categories (2) and (4)], the AF and d-SC orders tend to exclude each other, whereas in the regime of type-I AF [$t'/t \gtrsim 0$, categories (1) and (3)], the two orders are likely to coexist. This is the same tendency as that of the Hubbard model.[16]

Before studying the features of each category, we introduce common terminologies and an empirical law. If $E_A < E_B$ (A, B=AF or d-SC) for the pure states, we call the order A (B) the leading (subordinate) order. In all categories (1)–(4), the leading order necessarily arises in the mixed state Ψ_{mix}, if the leading order arises in the pure state with the same model parameter set ($t'/t, \delta$).

In category (1) [e.g., ($t'/t, \delta$) = (0.2, 0.08)], the leading and subordinate orders are the type-I AF and d-SC, respectively. According to the above law, the AF order of type-I arises in Ψ_{mix}; the problem is whether the d-SC order can simultaneously arise or not. Actually, the d-SC order coexists with the AF order in Ψ_{mix} as in Fig. 14(b). Let us consider the mechanism of the coexistence. Figure 15 shows the contour maps of $n(\mathbf{k})$ for the three kinds of Ψ. As described in Sect. 3.2, the pure AF state (left panel) has pocket FSs near antinodal [($\pm\pi, 0$), ($0, \pm\pi$)] and exhibits a gap in the other region of $\mathbf{k}$. In the pure d-SC state (middle panel), a SC gap opens except in the nodal directions ($k_y = \pm k_x$), where Fermi points appear near ($\pm\pi/2, \pm\pi/2$). As mentioned in Sect. 3.1 and in the previous paper,[16] the occurence of d-SC as the subordinate order requires the FSs which are connected with the scattering vector $\mathbf{Q} = (\pi, \pi)$ in the leading-order (AF) state, especially, near antinodal owing to the largest $d_{x^2-y^2}$-wave gap and density of state. In category (1), the pocket FSs in Fig. 15(a) meet this requirement. Consequently, the d-SC order arises in Ψ_{mix} and the d-SC gap opens at the loci of pocket FS near antinodal.
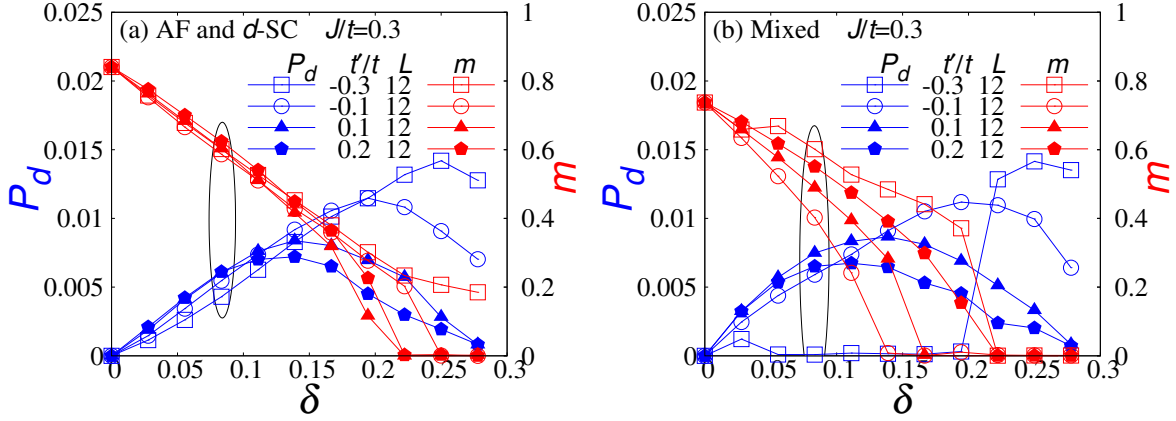

Fig. 15. (Color online) Contour maps of momentum distribution function $n(\mathbf{k})$ of (a) Ψ_{AF}, (b) Ψ_d, and (c) Ψ_{mix} for $(t'/t, \delta) = (0.2, \sim 0.08)$, a typical case of category (1) [E_{AF} (type-I) $< E_d$], in the first Brillouin zone. The arrow in (a) indicate the $\mathbf{Q}$ vector connecting two pocket FSs.

Fig. 14. (Color online) Doping-rate dependence of order parameters of d-SC (P_d, left axis) and AF (m, right axis). In (a), P_d (m) is calculated using the pure state Ψ_d (Ψ_{AF}). In (b), both P_d and m are calculated simultaneously using the mixed state Ψ_{mix}. The rings indicate $\delta = 0.08$ for explanation.
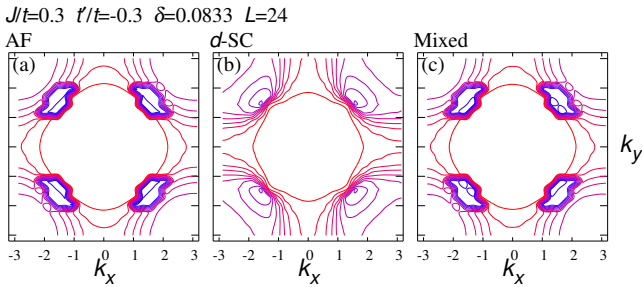

Fig. 16. (Color online) Contour maps similar to Fig. 15 but for $(t'/t, \delta) = (-0.3, \sim 0.08)$, a typical case of category (2) [E_{AF} (type-II) $< E_d$].
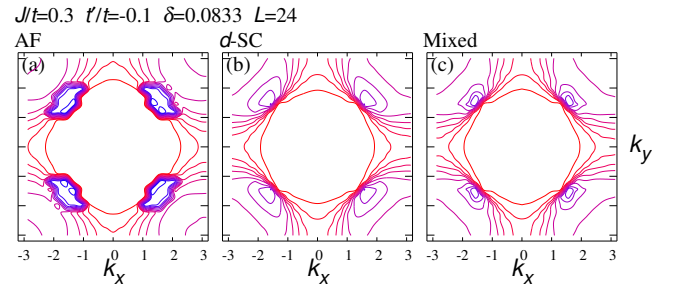

Fig. 18. (Color online) Contour maps similar to Fig. 15 but for $(t'/t, \delta) = (-0.1, \sim 0.08)$, a typical case of category (4) [$E_d < E_{AF}$ (type-II)].
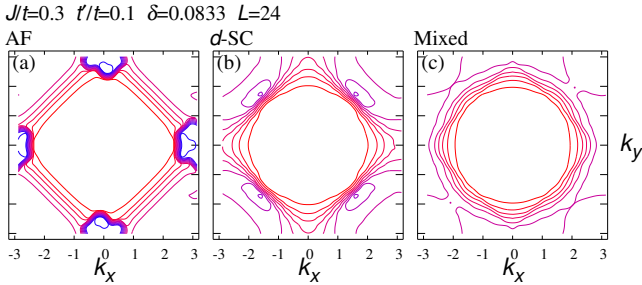

Fig. 17. (Color online) Contour maps similar to Fig. 15 but for $(t'/t, \delta) = (0.1, \sim 0.08)$, a typical case of category (3) [$E_d < E_{AF}$ (type-I)].

The resultant state Ψ_{mix} comes to have both orders and becomes a fully gapped state, as shown in Fig. 15(c).

In category (2) [e.g., $(t'/t, \delta) = (-0.3, 0.08)$], because the leading order is AF, the type-II AF order arises in Ψ_{mix}. In this case, the loci of FSs in Ψ_{AF} are in the nodal directions as shown in Fig. 16(a); a scattering vector **Q** to create the d-SC order cannot be placed between two antinodals. As a result, the d-SC order does not arise, and the resultant state Ψ_{mix} remains the pure AF state [Fig. 16(c)]. Namely, the d-SC order is excluded. The mechanisms in categories (1) and (2) are basically the same as those for the strongly correlated Hubbard model.[16] Comparing with Ref. 25 (See Tables I and II), we notice that the independence of t_η^{AF} and t_η^{SC} is crucial for this exclusivity.

In category (3) [e.g., $(t'/t, \delta) = (0.1, 0.08)$], the d-SC order necessarily appears, because it is the leading order. In this case, the situation of FSs of Ψ_{AF} and Ψ_d [Figs. 17(a) and 17(b)] is similar to category (1). Therefore, the two orders

are ready to coexist in Ψ_{mix} by using different parts of $n(\mathbf{k})$, resulting in a full gap as shown in Fig. 17(c). Because the leading order is d-SC in category (3), the subordinate order AF is weakened to some extent. This tendency contrasts with that of category (1).

In category (4), the leading order is d-SC, and the FS in Ψ_{AF} is type-II. The situation of $n(\mathbf{k})$ in Ψ_{AF} and Ψ_d [Fig. 18] is similar to that of category (2) [Fig. 16]. Therefore, the two orders tends to exclude each other, and the subordinate AF order is weakened ($\delta = 0.08$) or removed for high doping rates in Ψ_{mix} as in Fig. 14(b). Consequently, $n(\mathbf{k})$ of Ψ_{mix} becomes akin to $n(\mathbf{k})$ of Ψ_d as seen in Figs. 18(b) and 18(c). A point different from category (2) is that the subordinate order (AF) tends to be excluded not completely in Ψ_{mix}. This is probably because the nesting condition to be satisfied for the AF order is less strict than the condition for d-SC.

The above aspect of interplay between the AF and d-SC orders is more clearly revealed in J/t dependence of P_d and m. In the following, we focus on the cases of $\delta = 0.08$. We start with the type-I regime [$t'/t \gtrsim 0$, categories (1) and (3)]. Shown in Figs. 19(a) is J/t dependence of the energy difference between the two pure states ΔE [Eq. (31)]. As J/t increases, $\Delta E/t$ becomes negative at J_0/t (~ 0.2 for $t'/t = 0.1$, ~ 0.55 for $t'/t = 0.2$), where the stable state switches from AF to d-SC. Shown in Fig. 19(b) is J/t dependence of P_d and m simultaneously measured using Ψ_{mix}. As J/t increases from zero, both P_d and m rapidly increase and exhibit no anomaly near $J = J_0$; some inflection at $J/t \sim 0.15$ not only for $t'/t = 0.1$ but for 0.2 probably reflects the rapid variation of the states. Note that the subordinate order never vanishes both for $J < J_0$ (P_d) and $J > J_0$ (m). Thus, in the type-I regime,
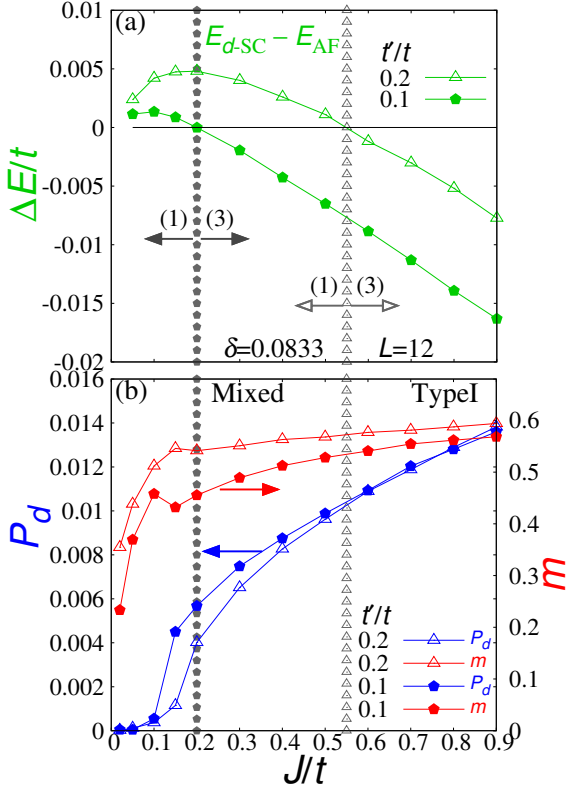
Fig. 19. (Color online) (a) The energy difference between the two pure states [Eq. (31)] and (b) the order parameters calculated using Ψ_{mix} are plotted as functions of J/t for typical values of t'/t in the type-I AF regime. As guides, the points where $\Delta E/t$ crosses zero (J_0/t) are indicated by the gray pentagons and open triangles for $t'/t = 0.1$ and 0.2, respectively. The regimes of $J < J_0$ and $J > J_0$ belong to categories (1) and (3), respectively, as shown by arrows for each t'/t.
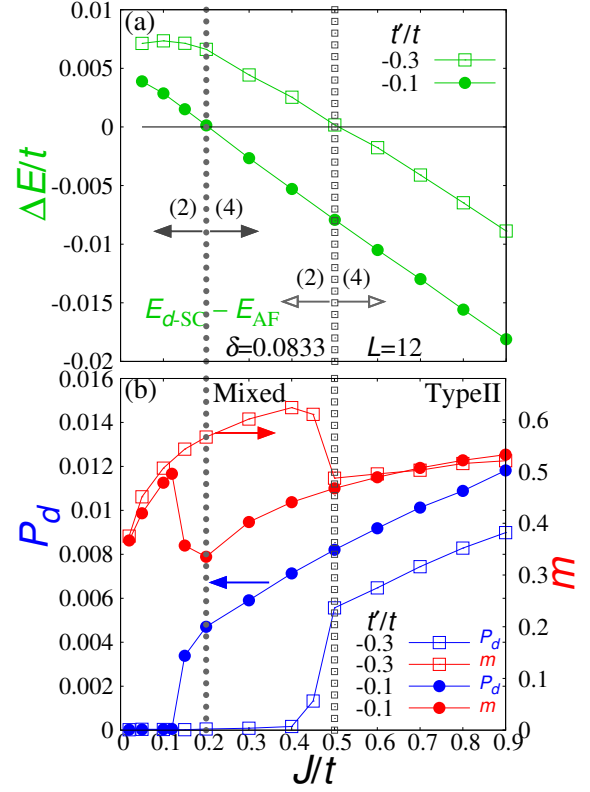
the two orders tend to coexist.

In Fig. 20, ΔE [in (a)], P_d and m [in (b)] are similarly shown for the type-II regime ($t'/t \lesssim 0$). In contrast with the type-I cases, the behavior of both P_d and m anomalously changes near $J = J_0$. For $J \lesssim J_0$ [category (2)], the subordinate d-SC order is completely suppressed by the leading AF order. For $J \gtrsim J_0$, [category (4)] the leading d-SC order suddenly increases and the subordinate AF order drops near $J = J_0$. In this regime, substantial magnitude of m is preserved in Ψ_{AF}. Anyway, in the type-II regime, the two orders tend to exclude each other.

As a summary, we construct a t'-δ phase diagram of AF and d-SC orders for $J/t = 0.3$ using the mixed state Ψ_{mix} (Fig. 21). Compared to the corresponding phase diagram of the Hubbard (t-t'-U) model for $U/t = 12$ (Fig. 27 in Ref. 16), the aspect of AF is quite similar, but the aspect of d-SC is different in that its area greatly expands from a part of type-II area to a large range of type-I area. And that the d-SC order coexists with the AF order even in the type-II area. Another characteristic point is that there is no area where a state is unstable toward PS. The behavior of $\chi_c > 0$ in Ψ_{mix} (cf. Sect. 3.2) coincides with previous results.[25,32]

When we consider the correspondence with the Hubbard model with $U/t = 12$, the value $J/t = 0.3$ seems too large in that the d-SC order excessively appears, but too small in that
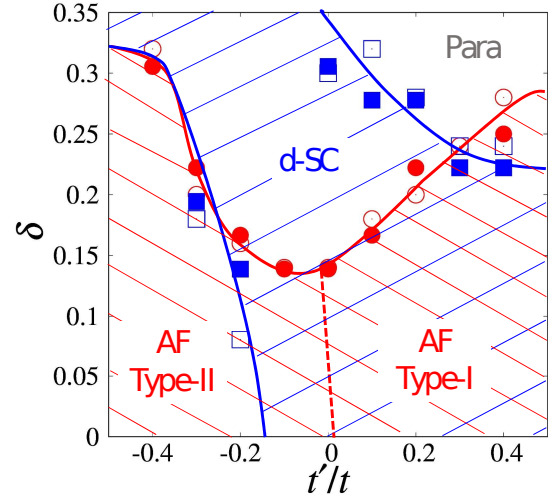

Fig. 20. (Color online) The same quantities as in Fig. 19 are plotted but for the values of t'/t in the type-II AF regime: $t'/t = -0.1$ and -0.3. The regimes of $J < J_0$ and $J > J_0$ belong to categories (2) and (4), respectively.

Fig. 21. Phase diagram of AF and d-SC orders in t'-δ space constructed using Ψ_{mix} for $J/t = 0.3$. The AF order exists under the bold red curve (guide line), and the d-SC order appears in the area between the two bold blue curves. Solid (open) symbols indicate the boundary points determined using the systems of $L = 12$ (10). In the whole area, all states are stable against PS.

PS does not occur. The correspondence is not simple. This is possibly because the three-site (pair-hopping) and J' terms are disregarded in the model. Anyway, in the context of cuprates, the main problem remains—why the robust AF order survives up to high doping rates in theory.

5. Summary

As an extension of previous work for the Hubbard model,[16] we studied band-renormalization effects (BRE) on the interplay between AF and d-SC orders in the t-t'-J model, which is expected to more favor the d-SC order than the Hubbard model. To reliably treat strong correlation of the t-J model, a VMC method was used. We mainly discussed the case of $J/t = 0.3$ realistic values for cuprate SC. We summarize the main results below.

(i) BR modifies the properties of d-SC only slightly but greatly stabilizes the AF state, especially, for large values of $|t'/t|$ (Table III). Consequently, the t'-δ phase diagram is largely modified; the AF order prevails in almost whole underdoped range (Fig. 21), similarly to the Hubbard case.

(ii) The metallic AF order for $\delta > 0$ in Ψ_{AF} is classified into two types according to $t' > t'_L$ (type-I) or $t' < t'_L$ (type-II), where t'_L/t (~ 0) is a Lifshitz transition point (Fig. 10). As t'/t decreases, the loci of the pocket Fermi surface switch at $t' = t'_L$ from antinodal [$\sim (\pi, 0)$] to the nodal directions [$\sim (\pi/2, \pi/2)$]. This distinction of AF type plays a crucial role for coexistence/exclusivity of the AF and d-SC orders in Ψ_{mix}. The two orders tend to coexist (exclude each other) in the area of type-I (II) AF for the same reason as in the Hubbard model,[16] in short, compatibility of the electronic states.

(iii) In contrast with the Hubbard model with $U/t = 12$, the pure d-SC state becomes more stable than the pure AF state in the underdoped regime ($\delta \lesssim 0.16$) for small values of $|t'/t|$, namely, d-SC becomes the leading order. As a result, it is convenient for discussing coexistence/exclusivity that the t'-δ space is divided into four domains (categories) according to whether or not $E_{AF} < E_d$ in addition to whether or not $t' < t_L$. The area of coexistence comes to appear in the regime of type-II AF ($-0.2 \lesssim t'/t \lesssim 0$), besides widely in the type-I regime ($t'/t > 0$) (Fig. 21).

(iv) For $J/t = 0.3$, any state considered here is stable against PS (Fig. 11), in contrast with for the Hubbard model with $U/t = 12$, where states with the AF order is unstable toward PS near $t'/t = 0$. However, from analysis of energy components, both AF and d-SC states probably become unstable toward PS for larger values of J/t.

On the basis of (i) and (iii), we repeat that the problem of coexistence/exclusivity largely depends on the value of t'/t and BRE should be properly introduced for $t'/t \sim \pm 0.3$ (Table I). Regarding (iv), PS in the t-J model is a long-standing problem. We will reconsider it in another publication. We concentrated on the interplay between the AF and d-SC orders; it is important to study interplay among other low-energy states such as staggered-flux[3,57,58] and striped states.[59]

The tendency toward predominant AF long-range orders has been reported not only for the single-band models discussed above but also for the d-p model.[60,61] In addition to this predominant AF, some results are inconsistent with the behavior of cuprates: For instance, except for the multilayered systems,[62] the AF and d-SC long-range orders do not coexist and the AF states are always insulating. These points suggest that the uniform models are possibly insufficient to describe cuprate SCs. One possibility for reconciling the inconsistency with experiments is that some disorders such as the impurity potential of carrier dopants, which is inherent in cuprates, destabilize the long-range AF order but affect the
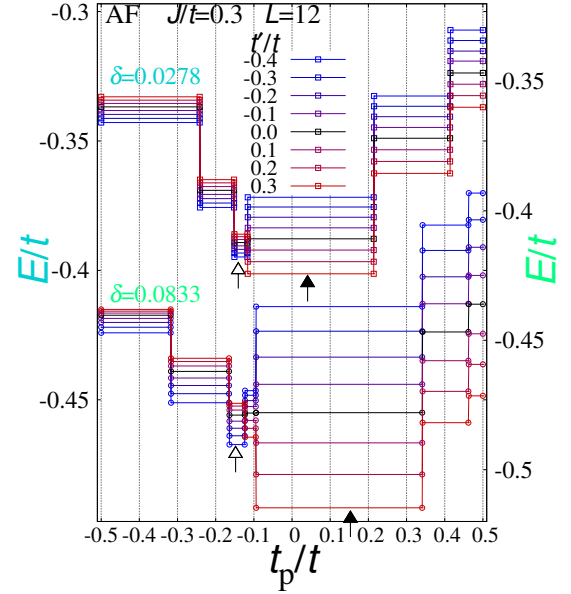

Fig. A·1. (Color online) t_p/t (parameter for determining $\{k\}_{occ}$) dependence of total energy per site for the AF state is shown for various values of a model parameter t'/t and two doping rates δ. The system size is $L = 12$. The variational parameters except for t_p/t are optimized for each model parameter set. The ranges of t_p/t that give the minima of E/t are indicated by filled (for Type-I AF) and empty (for Type-II AF) arrows for each δ.

d-SC order only slightly. Inhomogeniety allows static short-range AF orders. We will address such subjects elsewhere.[63]

Appendix A: Optimization of Occupied k-Points $\{k\}_{occ}$ in Normal, AF, and Mixed States

In this Appendix, we describe the details of how we actually optimize Ψ_N, Ψ_{AF} and Ψ_{mix} for finite systems in this study. The operation in band renormalization for finite-size systems is composed of two elements:[16] (i) Optimization of the energy dispersion ε_k itself, and (ii) optimization of $\{k\}_{occ}$ (the set of discrete k-points occupied by electrons), which is usually obtained by filling the k-points with electrons in the order of small ε_k optimized in (i).[64] These two elements merge in the thermodynamic limit, but it is convenient to treat the two elements independently for finite systems for technical reasons.

In optimizing the band parameters t_η^{AF}/t for finite systems, E/t becomes discontinuous as a function of t_η^{AF}/t at specific values $t_\eta^{(i)}/t$ ($i = 1, 2, \cdots$), owing to the discrete k-points. Namely, $\{k\}_{occ}$ switches from one to another at $t_\eta^{(i)}/t$. Furthermore, ε_k sometimes becomes almost constant in the ranges between two discontinuities, say $t_\eta^{(1)} < t_\eta < t_\eta^{(2)}$. As a result, it becomes inconvenient to apply ordinary optimization tools based on the derivative of ε_k, such as the quasi-Newton method and the stochastic reconfiguration method.

To overcome this difficulty, we follow the next prescription in this study. In the process of (ii), we generate $\{k\}_{occ}$ independently of ε_k^{AF} or t_η^{AF}/t and fix it at a certain configu-

ration. Then, E/t becomes continuous as a function of every variational parameter, and the ordinary optimization tools become applicable. Comparing E/t thus optimized for a certain $\{\mathbf{k}\}_{\mathrm{occ}}$ with those optimized for other $\{\mathbf{k}\}_{\mathrm{occ}}$, we can determine the optimized energy and wave function. In this process, it is not realistic that one checks all possible $\{\mathbf{k}\}_{\mathrm{occ}}$ one by one, because the number of $\{\mathbf{k}\}_{\mathrm{occ}}$ grows exponentially as the system-size increases. For the present case, we found that almost all optimized $\{\mathbf{k}\}_{\mathrm{occ}}$ for small L are included in those generated by $\varepsilon_{\mathbf{k}}$ up to the diagonal hopping. Therefore, we consider only $\{\mathbf{k}\}_{\mathrm{occ}}$ generated by

$$\varepsilon_{\mathbf{k}}^{(p)} = -2t\left(\cos k_x + \cos k_y\right) - 4t_{\mathrm{p}} \cos k_x \cos k_y, \qquad (\mathrm{A\cdot1})$$

in a proper range of t_{p}/t, instead of $\varepsilon_{\mathbf{k}}^{\mathrm{AF}}$ in Eq. (17) or $E_{\mathbf{k}}^{\mathrm{AF}} = U/2 - \sqrt{(\varepsilon_{\mathbf{k}}^{\mathrm{AF}})^2 + \Delta_{\mathrm{AF}}^2}$. Here, t_{p}/t is a kind of variational parameter that optimizes $\{\mathbf{k}\}_{\mathrm{occ}}$ and is independent of $\varepsilon_{\mathbf{k}}^{\mathrm{AF}}$. Thereby, the number of $\{\mathbf{k}\}_{\mathrm{occ}}$ to be checked is greatly reduced. In Fig. A·1, we show the t_{p}/t dependence of variational energy per site for the AF state ($L = 12$), where all the residual variational parameters including t_{η}^{AF}/t are optimized. In the range of t_{p}/t corresponding to a certain $\{\mathbf{k}\}_{\mathrm{occ}}$, E/t is constant. The optimized $\{\mathbf{k}\}_{\mathrm{occ}}$ is determined by finding the range with the lowest E/t. Shown in this figure are the data for $\delta \sim 0.03$ and 0.08, and the model parameter $t'/t = -0.4$ – $+0.3$ for each δ. We find for $\delta = 0.083$ that the optimized $\{\mathbf{k}\}_{\mathrm{occ}}$ is generated using $t_{\mathrm{p}}/t = -0.15$ [0] (or nearby t_{p}/t in the same range) for $t'/t < 0$ (type-II AF) [$t'/t > 0$ (type-I AF)] as indicated with an open [a solid] arrow.

We apply this scheme to all cases of $L = 10$ and 12 for Ψ_{N}, Ψ_{AF}, and Ψ_{mix}. In some cases, however, it was found that the true optimized $\{\mathbf{k}\}_{\mathrm{occ}}$ is not generated within the above scheme, especially, for considerably large $|t'/t|$ and δ. In such cases, we search within several plausible $\{\mathbf{k}\}_{\mathrm{occ}}$ on the basis of the optimized data for small L. The above scheme, if the correct $\{\mathbf{k}\}_{\mathrm{occ}}$ is obtained, is being an optimization in a wider parameter range in the sense that $\varepsilon_{\mathbf{k}}$ and $\{\mathbf{k}\}_{\mathrm{occ}}$ are independently optimized; actually, a parameter t_{p}/t is added. However, it remains within the finite-size correction, because the two elements merge for $L \to \infty$.

Appendix B: Choice of $\{\mathbf{k}\}_{\mathrm{occ}}$ as Leading Role of BRE

As discussed in Sects. 3.1 and 3.2, BRE plays a crucial role in reducing E_{AF} for large $|t'/t|$. In this Appendix, we argue that the choice of $\{\mathbf{k}\}_{\mathrm{occ}}$ (not optimizing $\varepsilon_{\mathbf{k}}^{\mathrm{AF}}$) primarily contributes to this energy reduction and other properties by analyzing the behavior owing to $\{\mathbf{k}\}_{\mathrm{occ}}$ (or t_{p}) and to $\varepsilon_{\mathbf{k}}^{\mathrm{AF}}$ [or t_{η} ($= t_{\eta}^{\mathrm{AF}}$), $\eta = 1$–4], and by comparing with results of the previous study[16] in which $\{\mathbf{k}\}_{\mathrm{occ}}$ and $\varepsilon_{\mathbf{k}}^{\mathrm{AF}}$ depend on each other.

Shown in Fig. B·1 is the t'/t dependence of the optimized band parameters t_{η} and the parameter t_{p}, which determines $\{\mathbf{k}\}_{\mathrm{occ}}$, for $\delta = 0.0833$. As described in Appendix A, t_{p} is determined independently of t_{η} in Ψ_{AF}. Corresponding results for the Hubbard model are presented in Fig. 13(b) in Ref. 16, in which, contrastively, $\{\mathbf{k}\}_{\mathrm{occ}}$ is determined according to $\varepsilon_{\mathbf{k}}^{\mathrm{AF}}$ (or t_{η}). Inversely speaking, available ranges of t_{η} are regulated by $\{\mathbf{k}\}_{\mathrm{occ}}$. The difference of models is irrelevant here. Comparing these two results for $t'/t > 0$, we find that the opitized values of t_{η} are virtually identical. In this regime of t'/t, the optimized $\{\mathbf{k}\}_{\mathrm{occ}}$ ($\equiv \{\mathbf{k}\}_{\mathrm{occ}}^{(p)}$) based on t_{p} is identical with $\{\mathbf{k}\}_{\mathrm{occ}}$
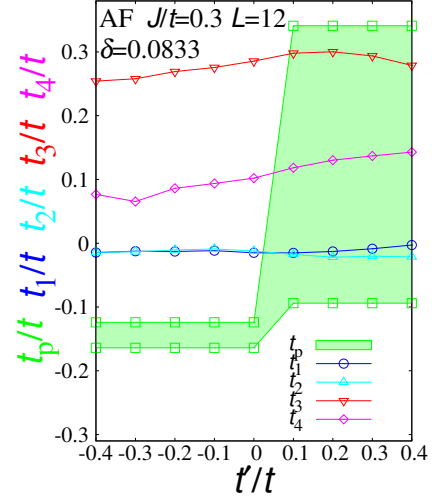

Fig. B·1. (Color online) t'/t dependence of optimized band parameters in Ψ_{AF}. The energy for a fixed t'/t becomes constant in certain ranges of t_{p} as explained in Appendix A; the optimized range of t_{p} is shown in green.

($\equiv \{\mathbf{k}\}_{\mathrm{occ}}^{(\varepsilon)}$) determined using the optimized t_{η}.

On the other hand for $t'/t < 0$, in Fig. B·1, the optimized range of t_{p}/t is switched to a different narrow one (~ -0.14), whereas the optimized t_{η} are smoothly extended from the regime of $t'/t > 0$. It follows that $\{\mathbf{k}\}_{\mathrm{occ}}^{(p)} \neq \{\mathbf{k}\}_{\mathrm{occ}}^{(\varepsilon)}$ for $t'/t < 0$. As discussed in Sect. 3.2, some properties of Ψ_{AF} are critically different between for $t'/t \gtrsim 0$ (type I) and $t'/t \lesssim 0$ (type II). Therefore, such properties are considered to be led by $\{\mathbf{k}\}_{\mathrm{occ}}$ or FS and not by $\varepsilon_{\mathbf{k}}^{\mathrm{AF}}$ itself. This predominance of $\{\mathbf{k}\}_{\mathrm{occ}}$ over $\varepsilon_{\mathbf{k}}^{\mathrm{AF}}$ can be seen in energy reduction. In contrast to the case in Fig. B·1, the optimized t_{η} in Fig. 13(b) in Ref 16 are switched to different values for $t'/t < 0$. This is because t_{η} are adjusted so as to satisfy $\{\mathbf{k}\}_{\mathrm{occ}}^{(\varepsilon)} = \{\mathbf{k}\}_{\mathrm{occ}}^{(p)}$. Namely, the optimization of $\{\mathbf{k}\}_{\mathrm{occ}}$ takes priority over that of $\varepsilon_{\mathbf{k}}^{\mathrm{AF}}$ in energy minimization. Thus, we can conclude that the reduction in E_{AF} and some relevant properties are primarily caused by FS renormalization, and not by the band form $\varepsilon_{\mathbf{k}}^{\mathrm{AF}}$ itself.

1) J. G. Bednorz and K. A. Müller, Z. Phys. B **64**, 189 (1986).
2) For the recent status of experimental research, see, for instance, articles in the special issue of J. Phys. Soc. Jpn. **81** vol. 1 (2012) on "Recent developments in superconductivity".
3) P. A. Lee, N. Nagaosa, and X.-G. Wen, Rev. Mod. Phys. **78**, 17 (2006).
4) M. Ogata and H. Fukuyama, Rep. Prog. Phys. **71**, 036501 (2008).
5) H. Yokoyama and H. Shiba, J. Phys. Soc. Jpn. **56**, 3570 (1987).
6) H. Yokoyama and H. Shiba, J. Phys. Soc. Jpn. **57**, 2482 (1988).
7) C. Gros, Ann. Phys. (New York) **189**, 53 (1989).
8) H. Yokoyama and M. Ogata, J. Phys. Soc. Jpn. **65**, 3615 (1996).
9) A. Paramekanti, M. Randeria, and N. Trivedi, Phys. Rev. B **70**, 054504 (2004).
10) P. W. Anderson, P. A. Lee, M. Randeria, T. M. Rice, N. Trivedi, and F. C. Zhang, J. Phys. Condens. Matter **16**, R755 (2004).
11) H. Yokoyama, M. Ogata, Y. Tanaka, K. Kobayashi, and H. Tsuchiura, J. Phys. Soc. Jpn. **82**, 014707 (2013).
12) Many other studies. See, for instance, literature in Refs. 3, 4, 10, and 11.
13) J. Otsuki, H. Hafermann, and A. I. Lichtenstein, Phys. Rev. B **90**, 235132 (2014).
14) T. Misawa and M. Imada, Phys. Rev. B **90**, 115137 (2014).
15) B.-X. Zheng and G. K.-L. Chan, Phys. Rev. B **93**, 035126 (2016).
16) R. Sato and H. Yokoyama, J. Phys. Soc. Jpn. **85**, 074701 (2016).

17) P. W. Anderson, Science **235**, 1196 (1987); F. C. Zhang and T. M. Rice, Phys. Rev. B **37**, 3759(R) (1988).

18) A. B. Harris and R. V. Lange, Phys. Rev. **157**, 295 (1967).

19) J. E. Hirsch, Phys. Rev. Lett. **54**, 1317 (1985).

20) C. Gros, R. Joynt, and T. M. Rice, Phys. Rev. B **36**, 381 (1987).

21) C. T. Shih, T. K. Lee, R. Eder, C.-Y. Mou, and Y. C. Chen, Phys. Rev. Lett. **92**, 227002 (2004).

22) L. Spanu, M. Lugas, F. Becca, and S. Sorella, Phys. Rev. B **77**, 024510 (2008).

23) T. Watanabe, H. Yokoyama, K. Shigeta, and M. Ogata, New J. Phys. **11**, 075011 (2009).

24) S. Pathak, V. B. Shenoy, M. Randeria, and N. Trivedi, Phys. Rev. Lett. **102**, 017002 (2009).

25) K. Kobayashi, R. Sato, and H. Yokoyama, Phys. Proc. **81**, 1 (2016).

26) W. L. McMillan, Phys. Rev. **138**, A442 (1965); D. Ceperley, G. V. Chester, K. H. Kalos, Phys. Rev. B **16**, 3081 (1977); H. Yokoyama and H. Shiba, J. Phys. Soc. Jpn. **56**, 1490 (1987); C. J. Umrigar, K. G. Wilson, and J. W. Wilkins, Phys. Rev. Lett. **60**, 1719 (1988).

27) T. K. Lee and S. Feng, Phys. Rev. B **38**, 11809 (1988).

28) T. Giamarchi and C. Lhuillier, Phys. Rev. B **43**, 12943 (1991).

29) A. Himeda and M. Ogata, Phys. Rev. B **60**, R9935 (1999).

30) D. A. Ivanov, Phys. Rev. B **70**, 104503 (2004).

31) C. T. Shih, Y. C. Chen, C. P. Chou, and T. K. Lee, Phys. Rev. B **70**, 220502 (2004).

32) M. Lugas, L. Spanu, F. Becca, and S. Sorella, Phys. Rev. B **74**, 165122 (2006).

33) K. Kobayashi and H. Yokoyama, JPS Conf. Proc. **3**, 015012 (2014); Phys. Proc. **58**, 22 (2014).

34) M. Ogata and A. Himeda, J. Phys. Soc. Jpn. **72**, 374 (2003).

35) L. F. Tocchio, F. Becca, and S. Sorella, Phys. Rev. B **94**, 195126 (2016).

36) R. Sato and H. Yokoyama, JPSCP **871**, 012014 (2017).

37) For instance, T. Tohyama and S. Maekawa, Supercond. Sci. Technol. **13**, R17 (2000).

38) R. Raimondi, J. H. Jefferson, and L. F. Feiner, Phys. Rev. B **53**, 8774 (1996); L. F. Feiner, J. H. Jefferson, and R. Raimondi, Phys. Rev. Lett. **76**, 4939 (1996).

39) E. Pavarini, I. Dasgupta, T. Saha-Dasupta, O. Jepsen, and O. K. Anderson, Phys. Rev. Lett. **87**, 047003 (2001).

40) R. Jastrow, Phys. Rev. **98**, 1479 (1955).

41) M. C. Gutzwiller: Phys. Rev. Lett. **10**, 159 (1963).

42) A. Himeda and M. Ogata: Phys. Rev. Lett. **85**, 4345 (2000).

43) For $t' \neq 0$ or $\delta > 0$, the HF solution deviates from the present form of Φ_{AF}. However, the present form is not inappropriate, because the optimized band is renormalized so as to satisfy the nesting condition. Actually, it is confirmed that the optimized energies of the present form and of the HF solution obtained by numerically diagonalizing $\mathcal{H}_{\text{MF}}$ coincide with each other in another context by Y. Toga (unpublished).

44) J. P. Bouchaud, A. Georges, and C. Lhuillier, J. Phys. (Paris) **49**, 553 (1988).

45) S. Sorella, Phys. Rev. B **64**, 024512 (2001).

46) K. Kobayashi and H. Yokoyama, Physica C **463-465**, 141 (2007); L. F. Tocchio, F. Becca, and C. Gros, Phys. Rev. B **86**, 035102 (2012).

47) D. J. Scalapino, Phys. Rev. **250**, 329 (1995).

48) For large values of $|t'/t|$ and δ, the optimization of $\{\mathbf{k}\}_{\text{occ}}$ is possibly incomplete within the scheme of a single parameter t_{p} described in Appendix A. The true E_{AF} is possibly smaller. As a result, the AF domain may somewhat expand to the large-δ direction for large $|t'/t|$. In contrast, in the mixed state, we determine $\{\mathbf{k}\}_{\text{occ}}$ using $\varepsilon_{\mathbf{k}}^{\text{AF}}$ (four-parameter scheme). Therefore, the choice of $\{\mathbf{k}\}_{\text{occ}}$ is more correct.

49) N. Trivedi and D. M. Ceperley, Phys. Rev. B **41**, 4552 (1990); K. J. Runge, Phys. Rev. B **45**, 12292 (1992).

50) S. Liang, B. Doucot, and P. W. Anderson, Phys. Rev. Lett. **61**, 365 (1988).

51) B. I. Shraiman and E. D. Siggia, Phys. Rev. Lett. **61**, 467 (1988).

52) R. J. Gooding, K. J. E. Vos, and P. W. Leung, Phys. Rev. B **50**, 12866 (1994).

53) For instance, T. K. Lee, C.-M. Ho, and N. Nagaosa, Phys. Rev. Lett. **90**, 067001 (2003); H. Kusunose and T. M. Rice, Phys. Rev. Lett. **91**, 186407 (2003); D. Senechal, P.-L. Lavertu, M.-A. Marois, and A.-M. S. Tremblay, Phys. Rev. Lett. **94**, 156404 (2005).

54) N. P. Armitage, *et al.*, Phys. Rev. Lett. **88**, 257001 (2002); N. P. Armitage, P. Fournier, and R. L. Greene, Rev. Mod. Phys. **82**, 2421 (2010).

55) For instance, F. Ronning, *et al.*, Science **282**, 2067 (1998).

56) R. Sato and H. Yokoyama, to be published in JPSCP , (2018).

57) H. Yokoyama, S. Tamura, and M. Ogata, J. Phys. Soc. Jpn. **85**, 124707 (2016).

58) K. Kobayashi and H. Yokoyama, JPS Conf. Proc. **871**, 012032 (2017); K. Kobayashi, H. Yokoyama, and Y. Toga, to be published in JPS Conf. Proc. (2018).

59) K. Kobayashi and H. Yokoyama, Low Temp. Phys. **117**, 199 (1999); A. Himeda, T. Kato and M. Ogata, Phys. Rev. Lett. **88**, 117001 (2002); P. Corboz, T. M. Rice, and M. Troyer, Phys. Rev. Lett. **113**, 046402 (2014); K. Ido, T. Ohgoe, and M. Imada, Phys. Rev. B **97**, 045138 (2018).

60) S. Tamura, Ph. D thesis, '*Variational Monte Carlo studies of d-p model*', (Tohoku University, 2016). [In Japanese]

61) T. Yanagisawa, I. Hase, M. Miyazaki, and K. Yamaji, to be published in JPS Conf. Proc. (2018).

62) H. Mukuda, S. Shimizu, A. Iyo, and Y. Kitaoka, J. Phys. Soc. Jpn. **81**, 011008 (2012); S. Shimizu, S.-i. Tabata, S. Iwai, H. Mukuda, Y. Kitaoka, P. M. Shirage, H. Kito, and A. Iyo, Phys. Rev. B **85**, 024528 (2012).

63) H. Yokoyama, R. Sato, and K. Kobayashi, to be published in JPS Conf. Proc. (2018), and in preparation.

64) The element (ii) is nonexistent for superconducting states, because all $\mathbf{k}$-points in the Brillouin zone are used.